Nano-sized BaSnO3 powder via a precursor route: Comparative study of sintering behaviour and mechanism of fine and coarse-grained powders

Roberto Köferstein, Lothar Jäger, Mandy Zenkner, Stefan G Ebbinghaus

Journal of the European Ceramic Society 29 (2009) 2317–2324

(doi:10.1016/j.jeurceramsoc.2009.01.026)

http://dx.doi.org/10.1016/j.jeurceramsoc.2009.01.026

Nano-sized $BaSnO_3$ powder via a precursor route. Comparative study of sintering behaviour and mechanism of fine and coarse-grained powders.

Roberto Köferstein*, Lothar Jäger, Mandy Zenkner, Stefan G. Ebbinghaus

Institut fürChemie/ Anorganische Chemie, Martin-Luther-Universität Halle-Wittenberg, Kurt-Mothes Strasse 2, D-06120 Halle, Germany

* Corresponding author. Tel.: +49-345-5525630; Fax: +49-345-5527028.
E-mail address: roberto.koeferstein@chemie.uni-halle.de

Abstract. Preparation of a very fine $BaSnO_3$ powder by calcination of a barium tin 1,2-ethanediolato complex precursor and its sintering behaviour are described herein. A rate controlled calcination process to 820 °C leads to a nm-sized $BaSnO_3$ powder with a specific surface area of S = 15.1 m^2/g ($d_{av.}$ = 55 nm). The powder has a slightly larger cell parameter of a = 412.22(7) pm compared to the single crystal value, which decreases with increasing calcination temperature and reaches the reference value above 1000 °C. The sintering behaviour is compared between fine- and coarse-grained $BaSnO_3$ powders. Corresponding powder compacts of the nano-sized $BaSnO_3$ achieve a relative density of 90 % after sintering at 1600 °C for 1 h and at 1500 °C and a soaking time of 30 h, whereas coarse-grained powder compacts reach only 80 % of the relative

density at 1650 °C (10 h). Furthermore, the shrinkage mechanisms of fine and coarse-grained powder compacts have been investigated and are discussed.

Keywords: Sintering (A); Perovskites (D); Precursor-organic (A); Grain size (B); Ceramics

1. Introduction

Barium stannate and its solid solutions (e.g. $BaTi_{1-x}Sn_xO_3$) have found important applications in materials science and technology due to their dielectric properties [1,2,3,4,5]. Pure and doped barium stannate can be used as material for semiconductor gas sensors. It has been reported that sensors based on $BaSnO_3$ are sensitive to a variety of gases, e.g. CO, O_2, C_2H_5OH, CH_3SH, LPG and NO_x [6,7,8,9,10,11,12]. Additionally, the results by *Borse* et al. [13,14] and *Yuan* et al. [15] suggest that $BaSnO_3$-based systems could be candidates for photocatalytic applications. *Mizoguchi* et al. [16] reported that $BaSnO_3$ exhibits strong near-infrared luminescence at room temperature.

The conventional mixed-oxide method requires high temperatures and results in coarse-grained powders [17,18]. Compacts of those powders show moderate densification behaviours. In the last years many preparation procedures have been published to obtain fine-grained $BaSnO_3$ powders at relatively low temperatures. Different hydrothermal methods or sol-gel processes have been developed [19,20,21,22,23]. A peroxide method was reported by *Pfaff* [24] to synthesise phase pure $BaSnO_3$. Recently, a lyothermal synthesis at 250 °C has been reported by *Lu* and *Schmidt* [25]. Various precursor complexes, coprecipitation- and polymerised complex methods have also been developed to obtain barium stannate powders [26,27,28,29]. Based on the exothermic reaction of suitable solids, self-propagating high temperature syntheses (SHS; also described as self-heat-sustained synthesis) are also used to prepare $BaSnO_3$ [30,31].

In ref. [29,32] we have reported on the preparation and structure of a precursor complex – $[Ba(HOC_2H_4OH)_4][Sn(OC_2H_4O)_3]$ – and its conversion into $BaSnO_3$. This precursor is suitable to form solid solutions of the type $[Ba(HOC_2H_4OH)_4][Ti_{1-x}Sn_x(OC_2H_4O)_3]$, which can be decomposed to phase pure fine-grained $BaTi_{1-x}Sn_xO_3$ powders [33].

This publication reports on the preparation of a nm-sized $BaSnO_3$ powder, prepared by the decomposition of a barium tin 1,2-ethanediolato complex precursor, the sintering behaviour and mechanism of resulting powder compacts. For comparative purposes, coarse-grained $BaSnO_3$ powders (mixed-oxide method) have also been studied.

2. Experimental

2.1. Material preparation

The preparation procedure for $[Ba(HOC_2H_4OH)_4][Sn(OC_2H_4O)_3]$ (**1**) has been described elsewhere [29,32]. For a better reproducibility we modified that procedure. $SnCl_4$ (0.10 mol; *Laborchemie Apolda*) was slowly added to ice-cold water (800 mL), and then a concentrated ammonia solution was added to adjust a pH value of 7–7.5. The precipitate was slowly filtered off and washed with water until the filtrate was almost free from Cl^- ions. A suspension of this wet precipitate ($SnO_2 \cdot n\ H_2O$) with $Ba(OH)_2 \cdot 8H_2O$ (0.10 mol; *Fluka*) and 800 mL 1,2-ethanediol was stirred overnight at room temperature in argon atmosphere. Thereafter the suspension was heated to remove water. Afterwards the reaction mixture was heated at 120–130 °C for 8 h. About ⅔ of the solvent was removed under reduced pressure at about 80 °C. The reaction mixture was then cooled and diluted with propan-2-ol. The crystalline precipitate of $[Ba(C_2H_6O_2)_4][Sn(C_2H_4O_2)_3]$ (**1**) was filtered off, washed with acetone and dried at room temperature. About 1.5 g of precursor **1** was calcined at 1200 °C and the resulting $BaSnO_3$ powder was dissolved in a 5M HCl solution at 35 °C. Chemical analyses

revealed a Ba/Sn ratio of 1.007 [34,35]. Calcination of **1** at 820 °C in static air led to a very fine $BaSnO_3$ powder (**1a**).

Additionally, $BaSnO_3$ powder was also prepared via a conventional mixed-oxide method. $BaCO_3$ (Sabed VL 600, *Solvay*) and SnO_2 (*Merck*) were milled with a molar ratio of 1:1 for 24 h using ZrO_2-balls in water (m_{powder}:m_{balls}:m_{water} = 1:1:4). After filtering off and drying the mixture was calcined in static air (rate 10 K/min) for 2 h at 1150 °C (**2**), at 1200 °C for 4 h (**3**), and at 1400 °C for 4 h (**4**) respectively. The Ba/Sn ratio of these mixed-oxide powders is 0.999 [34,35].

For the shrinkage and sintering behaviour the calcined powders (**1a**, **2**, **3**, **4**) were milled with ZrO_2-balls in propan-2-ol for 2 h (m_{powder}:m_{balls} = 1:4). After filtering and drying the powders were mixed with 5 mass% of a saturated aqueous solution of polyvinyl alcohol (PVA) as a pressing aid, then the powders were pressed to discs with a green density of about 3.4–3.6 g/cm^3.

2.2. Analytical methods

X-ray powder diffraction (XRD) patterns were recorded by a STADI MP diffractometer from *STOE* at 25 °C using Co$K\alpha_1$ radiation. The powder patterns were indexed and refined with the software suite WinXPOW [36] using the TREOR method [37]. Fourier transform attenuated total reflection infrared (ATR-IR) spectra in the range 4000–200 cm^{-1} (resolution: 4 cm^{-1}) were obtained using a Tensor 27 FT-IR spectrometer from *Bruker* with an ATR unit (MVP 2 Series from *Harrick*). Simultaneous thermogravimetric and mass spectrometry analysis (TG-MS) were carried out in flowing argon/oxygen (4:1) atmosphere using a STA 409C equipped with a quadrupole mass spectrometer Balzers QMS 421 (*Netzsch*, Al_2O_3-crucible, heating rate 20 K/min). Dilatometric investigations (shrinkage) were performed in a TMA 92-16.18 unit from *Setaram* and the densities of the discs were calculated assuming isotropic shrinkage

behaviour. The specific surface area was measured using nitrogen three-point BET (Nova 1000, *Quantachrome Corporation*). The average particle size was calculated assuming the powder particles were spherical or cubic in shape. Crystallite sizes were determined by XRD line broadening using the Scherrer equation [38] and the integral peak breadth. Scanning electron microscope images and energy dispersive X-ray analyses (EDX) were recorded by a *Philips* XL30 ESEM (Environmental Scanning Electron Microscope) and an embedded energy dispersive X-ray spectrometer from *Edax*.

3. Results and discussion

3.1. Powder Characterisation

In ref. [32] we have reported on a barium tin 1,2-ethanediolato complex precursor – $[Ba(HOC_2H_4OH)_4][Sn(OC_2H_4O)_3]$ (**1**) – and its decomposition to $BaSnO_3$ in detail. $BaSnO_3$ powder with a high specific surface area was obtained by decomposition of **1** by the following thermal treatment: heating to 500 °C with a heating rate of 10 K/min, slow heating with 1 K/min to 820 °C, dwelling time 180 min, followed by cooling at 3 K/min. The resulting white $BaSnO_3$ powder (**1a**) has a specific surface area of S = 15.1 m^2/g and an average particle size of $d_{av.}$ = 55 nm. Crystallite-size measurements by XRD line broadening [38] of the $BaSnO_3$ reflexions reveal a lower value of about $d_{crys.}$ = 26 nm. Discrepancies between the crystallite-/particle size estimated by the XRD line broadening and the specific surface area are reported and explained elsewhere [39]. The conventional white mixed-oxide powder **2** has a specific surface area of 4.6 m^2/g ($d_{av.}$ = 180 nm). SEM images of powder **1a** and **2** are shown in Fig. 1a,b and Fig. 1c,d, respectively. Both powders consist of cuboid-like particles.

XRD patterns of powder **1a** and **2** show reflexions of $BaSnO_3$ [40] (Fig. 2a,b). The diffraction pattern of powder **1a** reveals also traces of $BaCO_3$ [40]. IR measurements

(not shown) also reveal that powder **2** contains small traces of $BaCO_3$. XRD data (corrected by an internal standard) were indexed on the basis of a primitive cubic unit cell and the cell parameters were determined by least-square refinements. The reported reference lattice parameter for $BaSnO_3$ from XRD pattern is a = 411.63 pm [40]. Single crystal measurements by *Megaw* revealed a lattice parameter of a = 411.70 (15) pm (≡ 4.1085 kx) [41,42], which was also confirmed by *Smith* and *Welch* [43]. For powder **2** a lattice parameter of a = 411.69(4) pm was calculated, whereas a slightly larger lattice constant was found for powder **1a** (a = 412.22(7) pm). Thermal treatment (analogue procedure as described for **1a**) of precursor **1** at 900 °C results in a lattice dimension of a = 412.02(4) pm, at 1000 °C of a = 411.77(5) pm, and at 1100 °C of a = 411.63(6) pm. Ceramic bodies of **1a** and **2**, sintered at 1500 °C for 1 h (Fig. 2c,d), have lattice parameters of 411.64(1) pm (**1a**) and 411.67(3) pm (**2**), respectively. It can be seen a thermal treatment above 1000 °C leads to parameters which do not significantly change with increasing temperature. *Buscaglia* et al. [23] investigated the decomposition of $BaSn(OH)_6$ to $BaSnO_3$ and observed a decreasing cell parameter with increasing annealing temperature, too. By Raman spectroscopy they found that the powders, calcined at very low temperatures, retain a lot of hydroxyl groups inside the lattice, which cause the larger cell parameter. Our IR investigations (ATR-IR) do not reveal a clear evidence for O–H absorption bands. However, TG-MS measurements (Fig. 3) in an argon/oxygen atmosphere of powder **1a** and **2** show the release of CO_2 and H_2O during the thermal treatment to 1100 °C in both samples. The powders contain few amounts of $BaCO_3$ (see above), which cause the release of CO_2. Single thermogravimetric measurements up to 1100 °C in air (not shown) reveal mass losses of about 4.6 % (**1a**) and 0.86 % (**2**), respectively. The mass losses of the TG-MS measurements (see fig. 3) are less than of the single thermogravimetric measurements. At the beginning of the TG-MS measurement the equipment (including sample) was

flowed through with argon/oxygen gas for 1 h. The mass loss during this time was not recorded.

As can be seen, the release of H_2O takes place in two steps. The first peak at 227 °C (**1a**) and 211 °C (**2**) is attributed to the evolution of adsorbed water from the surface of the sample, whereas the second peak at about 380 °C (**1a**) and 477 °C (**2**) is caused by the dehydroxylation of OH groups inside the lattice (protonic defects) [44,45]. The amount of the detected CO_2 and H_2O in powder **2** is lower than in powder **1a**. Therefore, the low amount of OH lattice groups in powder **2** does not significantly influence the lattice constant. We suppose the low amount of protonic defects in powder **2** is created during the cooling phase in a furnace at ambient atmosphere. The amount of lattice OH groups in powder **1a** leads to an increase of the lattice parameter. Even a calcination time of 50 h at 820 °C results only in a very slight decrease of the lattice parameter to 412.10(4) pm. Protonic defects are investigated for $BaTiO_3$ and other titanates, very well [44,46,47,48,49,]. According to *Waser* [49] and *Hennings* et al. [50,51], the lattice OH groups, located on regular oxygen ion sites, cause a positive charge excess compensating by metal vacancies.

3.2. Shrinkage and sintering behaviour

Fig. 4 shows the dilatometric (non-isothermal) investigations to 1500 °C (heating rate 10 K/min) of powder compacts of **1a**, **2** and **3**. The theoretical density (single crystal density) of $BaSnO_3$ ceramics is 7.24 g/cm^3 [40].

The shrinkage process of powder compacts of **1a** starts at about 980 °C. A significant increase of the shrinkage rate is observed at 1130 °C and reaches a maximum at about 1183 °C. A second pronounced shrinkage process occurs at 1220 °C with a rate maximum at 1321 °C (-0.48 %/min). On the verge of the end of the heating period a last maximum of the shrinkage rate can be observed at 1489 °C (rate: -0.50 %/min). The

sample achieved a relative density of 69 % (4.99 g/cm^3) up to the end of the heating process.

Sample **2** slowly starts to shrink at 1055 °C, however a significant shrinkage process appears at about 1190 °C and shows two maxima of the shrinkage rate at 1365 °C and 1462 °C. The shrinkage rates at these maxima are -0.32 and -0.34 %/min. The shrinkage curve of **2** reveals an increasing densification to the end of the heating period and reaches 64 % (4.65 g/cm^3) of the theoretical density. Powder (**3**) (S = 2.6 m^2/g; $d_{ava.}$ = 319 nm) shows analogous shrinkage behaviour, however the whole shrinkage is lower. The maxima of the shrinkage rate appear at about 1430 °C (-0.20 %/min) and 1489 °C (-0.21 %/min). Up to 1500 °C the relative density reaches a value of 54 % (3.90 g/cm^3). The observed shrinkage rates at the maxima of **1a**, **2** and **3** ($d(\Delta L/L_0)/dt$ = -0.20 − -0.50 %/min) cannot be explained by diffusion processes alone. Diffusion as the dominant process causes shrinkage rates of about 10^{-4}–10^{-1} %/min [52]. Therefore, the observed shrinkage rates hint that the shrinkage is also caused by sliding processes of whole grains (also described as superplastic deformation [52,53]).

Isothermal dilatometric investigations allow to determine the dominant shrinkage mechanism, depending on the sintering time. The samples for these investigations were heated with a rate of 20 K/min. The heating rate was lowered to 10 K/min 50 K below the isothermal plateau was reached. The investigations for compacts of **1a** were carried out at several isothermal plateaus between 1150–1550 °C. The temperature ranges for powder **2** and **3** were set between 1220–1550 °C and 1400–1550 °C, respectively, because we did not observe a sufficient shrinkage below these ranges. The general approach of the isothermal investigations is reported elsewhere [39,54]. A representation of the logarithm of $\Delta L/L_0$ versus the logarithm of time (t) of the isothermal part (150 min) allows to verify the dominating shrinkage mechanism [54,55]. Fig. 5 exemplarily shows the isothermal curves for compacts of powder **1a**, **2** and **3** at

1400 °C. The isothermal shrinkage process is divided into two sections (different slopes) representing different shrinkage mechanisms [55] (see equation I).

$$\left(\frac{\Delta L}{L_0}\right)^{\frac{m}{2}} = -\frac{H}{2^m R^n} t \qquad \text{(I)}$$

Here, $\Delta L/L_0$ is the relative shrinkage, H is a function containing material parameters, R is the radius of the particles, t is the time, n and m are numerical exponents depending on the shrinkage mechanism ($m = 2 \rightarrow$ viscous flow; $m = 5 \rightarrow$ lattice diffusion from the grain boundary; $m = 6 \rightarrow$ grain boundary diffusion).

The first segment of the isothermal curves has a slope according to a shrinkage exponent of $m = 2$ indicating viscous flow as the major shrinkage mechanisms. The slope of the second segment is of the order of 0.32–0.5 and m is calculated to 4–6. Consequently, the shrinkage in the second stage is dominated by grain boundary diffusion and volume diffusion from the grain boundaries. It can be seen that the beginning of the shrinkage process is always dominated by viscous flow process, similar to the shrinkage behaviour of $BaTiO_3$-based ceramics [39,54,56]. Even a very coarse-grained mixed-oxide powder (**4**) (S = 1.02 m^2/g, $d_{av.}$ = 812 nm), investigated at 1550 °C, revealed also sliding processes in the first stage of shrinkage. A necessary presupposition for such sliding processes of whole grains is the existence of amorphous or defect-rich contact boundaries [52,57,58,59]. By means of the higher shrinkage rates and the better densification, sliding processes in compacts of **1a** are more dominant than in compacts of **2** and **3**. Powders with small particle sizes have a large amount of (defect-rich) grain boundaries, which are responsible for the appearance of sliding processes [57]. *Dror* et al. [56] described the grain boundaries as amorphous areas surrounding crystalline cores, which promote the sliding processes.

The above-mentioned classification of the appearing mechanisms (first → viscous flow, second → diffusion processes) is found for all investigated $BaSnO_3$ powders and temperatures.

Fig. 6 shows the final bulk densities of ceramic bodies of **1a** and **2** (calculated from their weight and geometric dimensions) depending on the sintering temperature and soaking time. In agreement with the results of other authors [17,60], green bodies of **2** show an insufficient shrinkage behaviour. Even at 1650 °C and a soaking time of 10 h we do not obtain dense ceramic bodies of ≥ 90 % of the relative density. SEM images of these bodies reveal a porous microstructure and show typical cubic-like grains [61] (Fig. 7a-c). However, from a temperature of 1600 °C and 10 h sintering, we observe a gradual change to globular-like or irregular grains (Fig. 7d). After sintering at 1450 °C and a soaking time of 1 h the ceramic bodies consist of grains between about 0.5–1.1 µm, which grow to 0.8–2.4 µm at 1650 °C. A prolonged soaking time of 10 h only leads to a grain growth to 1.3–7 µm at 1650 °C. In contrast, ceramic bodies of **1a** show a considerable better densification behaviour. Even at 1450 °C the ceramics have relative densities of 78 % (5.64 g/cm^3) and 83 % (6.01 g/cm^3) after sintering of 1 h and 10 h, respectively. A soaking time of 1 h and a sintering temperature of 1600 °C lead to ceramic bodies with a density of 90 % (6.50 g/cm^3) and a soaking time of 10 h raises the density to 92 % (6.69 g/cm^3). At a sintering temperature of 1650 °C we observe a slight increase of the densities to 6.67 g/cm^3 (92 %) and 6.75 g/cm^3 (93 %) after 1 h and 10 h, respectively. Sintering for 1 h leads to grain sizes of 0.65–2 µm (1450 °C), 0.9–2.8 µm (1550 °C), and 1.6–4 µm (1650 °C). After sintering of 10 h the grains grow from 0.9–2.6 µm (1450 °C) to 3–21 µm (1650 °C). Dense ceramic bodies, with grain sizes of 3–13 µm, can be also obtained after sintering at 1500 °C for 30 h (6.53 g/cm^3, 90 % rel. density). SEM images (Fig. 8) of ceramics of **1a** show, that these ceramics consist of

cubic-like grains up to about 1550 °C, however higher temperatures and soaking times gradually lead to an irregular shape of the grains (see Fig. 8 f.g).

In particular at sintering temperatures of 1600 and 1650 °C and longer soaking times, we observe a considerable mass loss of our ceramic bodies. Sintering at 1650°C of green bodies of **2** (disc, ∅ ≈ 6 mm, shortly preheated to 1650 °C to remove the PVA binder and possible traces of carbonates) for 10 h show a mass loss of about 16 %, which increases with raising sintering time (20 h) to 34 %. Samples of powder **1a** exhibit comparable mass losses. XRD patterns after these investigations reveal the samples consist of $BaSnO_3$ as the only crystalline phase. No second phases, e.g Ba_2SnO_4, could be detected. EDX analyses of ceramics (**2**) sintered at 1550 °C for 1 h, 1650 °C for 1 h and 20 h did not show any significant change in the Ba/Sn ratio. Therefore the mass loss primarily results from the evaporation of $BaSnO_3$ and is not caused by the evaporation of SnO_2 (decomposition) as observed at temperatures above 1800 °C [17].

4. Conclusion

The shrinkage behaviour and mechanism of fine and coarse-grained $BaSnO_3$ powder, prepared via a precursor and a mixed-oxide method were investigated. Calcination of a $[Ba(HOC_2H_4OH)_4][Sn(OC_2H_4O)_3]$ (**1**) precursor at 820 °C leads to a very fine $BaSnO_3$ powder (**1a**) with a specific surface area of 15.1 m^2/g ($d_{av.}$ = 55 nm) and a slightly larger cell parameter of a = 412.22(7) pm in comparison to the reference parameter. Coarse-grained samples (**2**), prepared by the mixed-oxide method (S = 4.6 m^2/g, $d_{av.}$ = 180 nm), show an insufficient sintering behaviour. Up to 1650 °C and a soaking of 10 h the compacts reaches a relative bulk density of 80 %. The porous ceramics consist of cubic grains. In contrast the fine-grained (nm-sized) powder **1a** reveal a considerable improvement of the sintering behaviour. Ceramics with at least 90 % of the single

crystal density can be obtained at 1600 °C or at 1500 °C and very long soaking time. Ceramic bodies with cubic grains are observed up to a sintering temperature of 1550 °C, higher temperatures leads to an irregular shape.

Isothermal dilatometric investigations show that the shrinkage of the investigated fine and coarse-grained powder compacts is characterized by sliding and diffusion processes. In particular, the beginning of the shrinkage process is always dominated by viscous flow, independent from the particle sizes of the powders. On the basis of the maxima of the shrinkage rates (non-isothermal), it can be seen the influence of the sliding processes decreases with increasing grain sizes of the powders.

Acknowledgements

The authors would like to thank Dr. Th. Müller for dilatometric and XRD measurements, F. Syrowatka for EDX measurements and Dr. J. Hanss (University of Augsburg) for TG-MS investigations. We are also grateful to Dr. D. Völtzke (Rauschert Hermsdorf GmbH) for his helpful discussions. Financial support by the Federal State Saxony-Anhalt (Cluster of Excellence "Nanostructured Materials") is gratefully acknowledged.

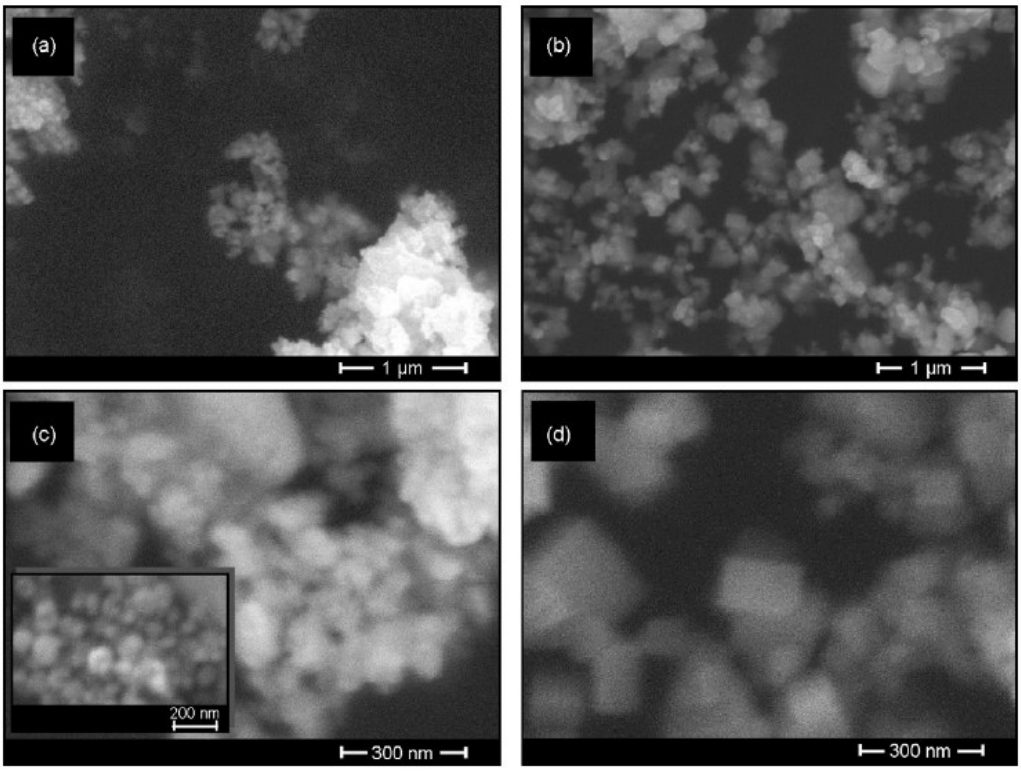

Fig. 1. SEM images of powders **1a** (a, b) and **2** (c, d) with different magnifications.

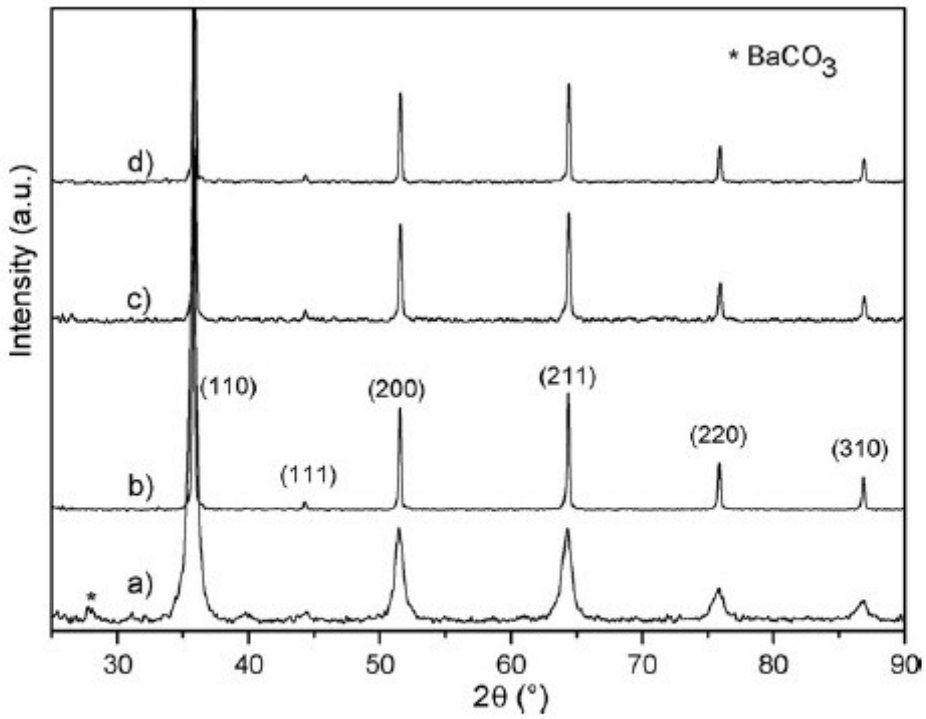

Fig. 2. X-ray powder diffraction patterns (recorded at 25 °C) of powders **1a** (a) and **2** (b), as well as corresponding ceramic bodies of **1a** (c) and **2** (d), sintered at 1500 °C for 1 h (rate: 10 K/min).

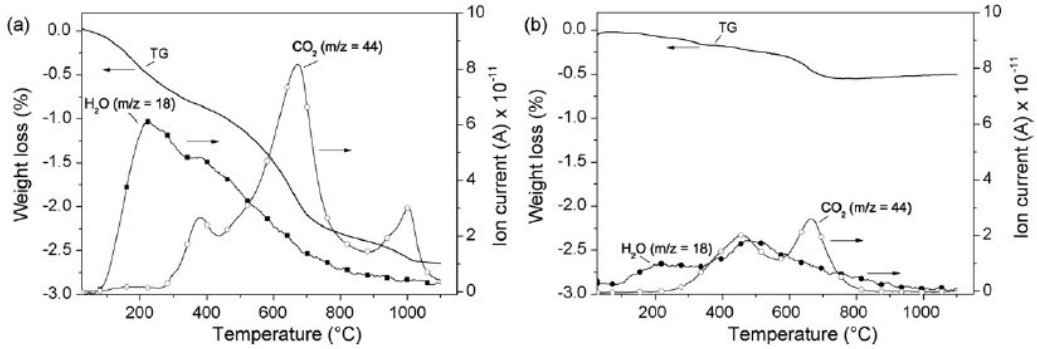

Fig. 3. TG–MS diagrams of powders **1a** (a) and **2** (b). Weighted samples: **1a**, 41.53 mg; **2**, 30.52 mg; heating rate 20 K/min.

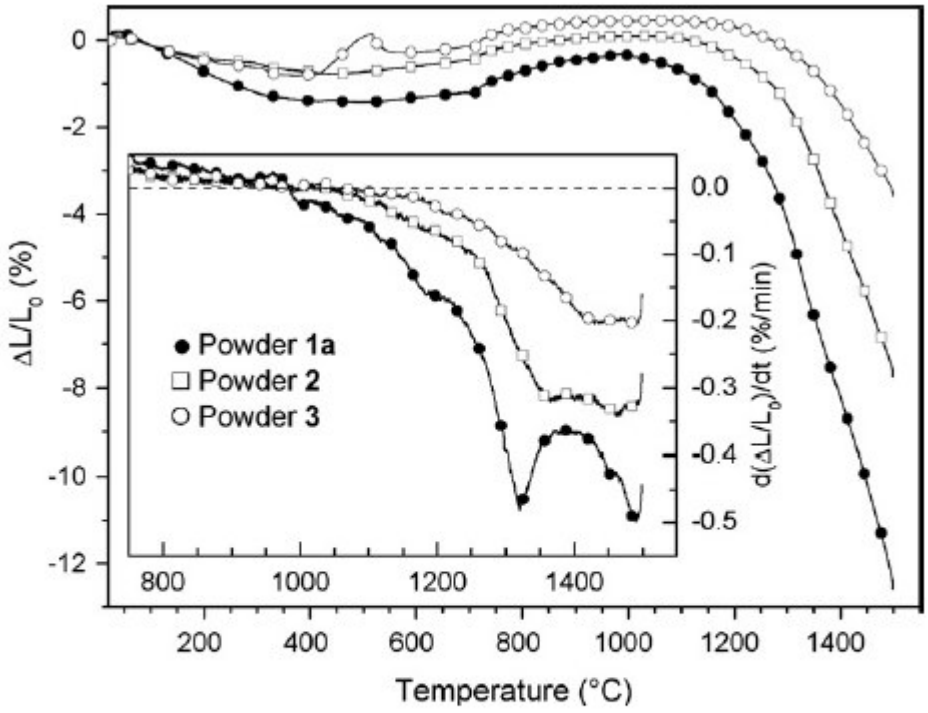

Fig. 4. Shrinkage behaviour (non-isothermal, heating rate 10 K/min) of green bodies of **1a**, **2**, and **3**, respectively. The inset shows the relative shrinkage rate ($d(\Delta L/L_0)/dt$) of these bodies (the green densities are; 3.3 g/cm^3 (**1a**), 3.6 g/cm^3 (**2**), and 3.5 g/cm^3 (**3**)). Every 100th data point is marked by a symbol.

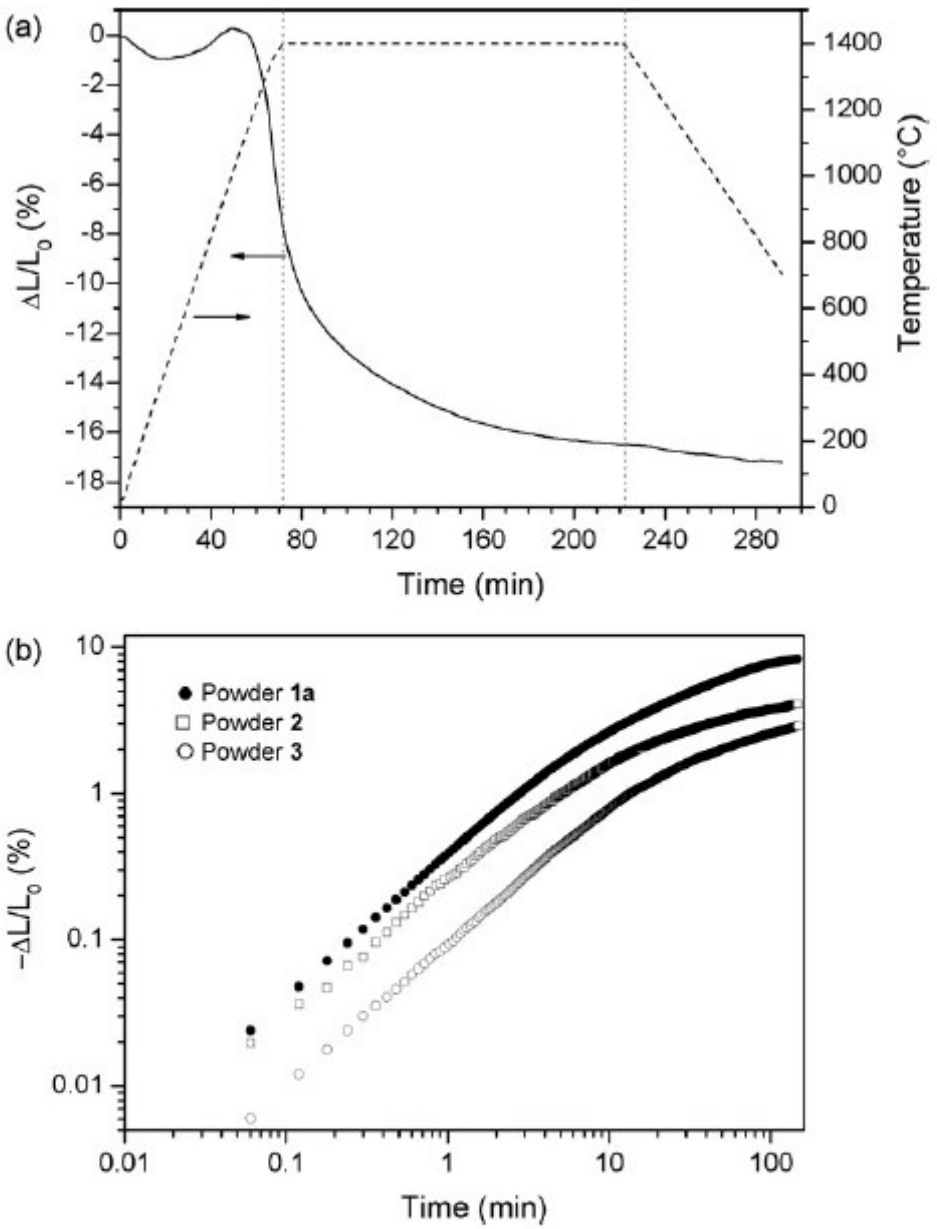

Fig. 5. Isothermal dilatometric investigations of powders **1a**, **2**, **3**, demonstrated at 1400 °C; (a) plot of the whole shrinkage curve (illustrated by the example of powder **1a**); (b) double logarithmic plot of the isothermal segments (the initial values of $\Delta L/L_0$ were set to zero).

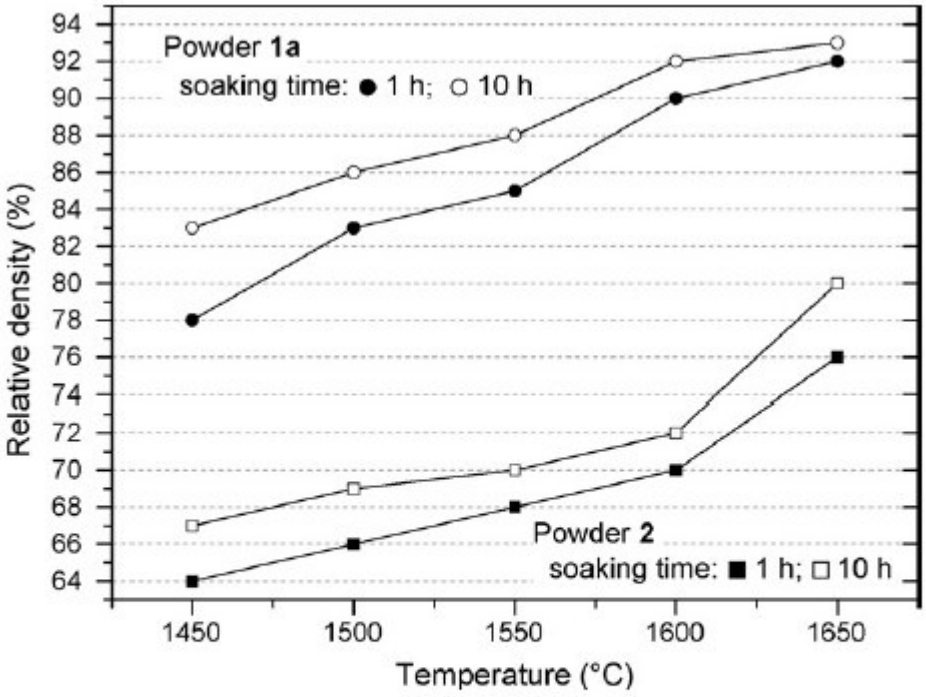

Fig. 6. Final densities of ceramic bodies of **1a** and **2** after an isothermal sintering process at various temperatures at the indicated soaking times in a muffle furnace (heating rate: 10 K/min). The relative densities are related to the theoretical density of 7.24 g/cm^3.

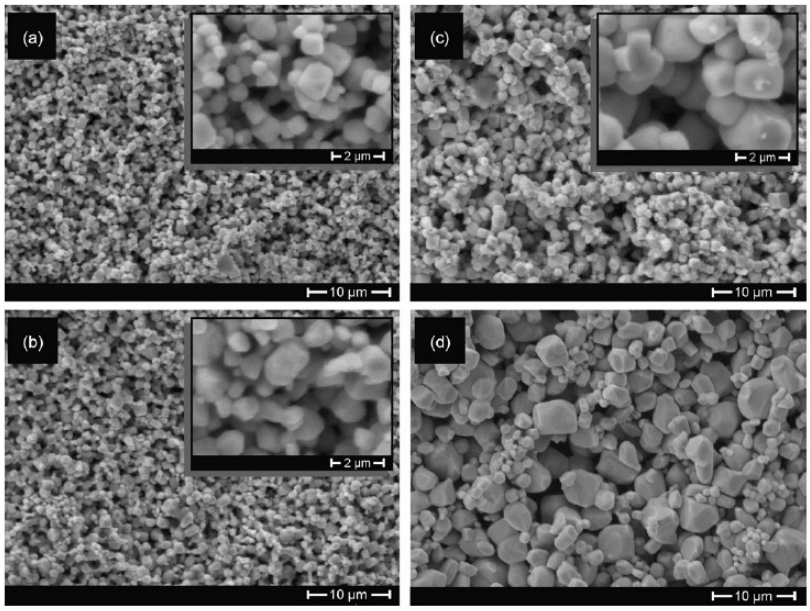

Fig. 7. SEM micrographs of the surfaces of ceramic bodies of **2** after various sintering temperatures and soaking times. (a) 1550 °C, 1 h; (b) 1600 °C, 1 h; (c) 1650 °C, 1 h; (d) 1600 °C, 10 h.

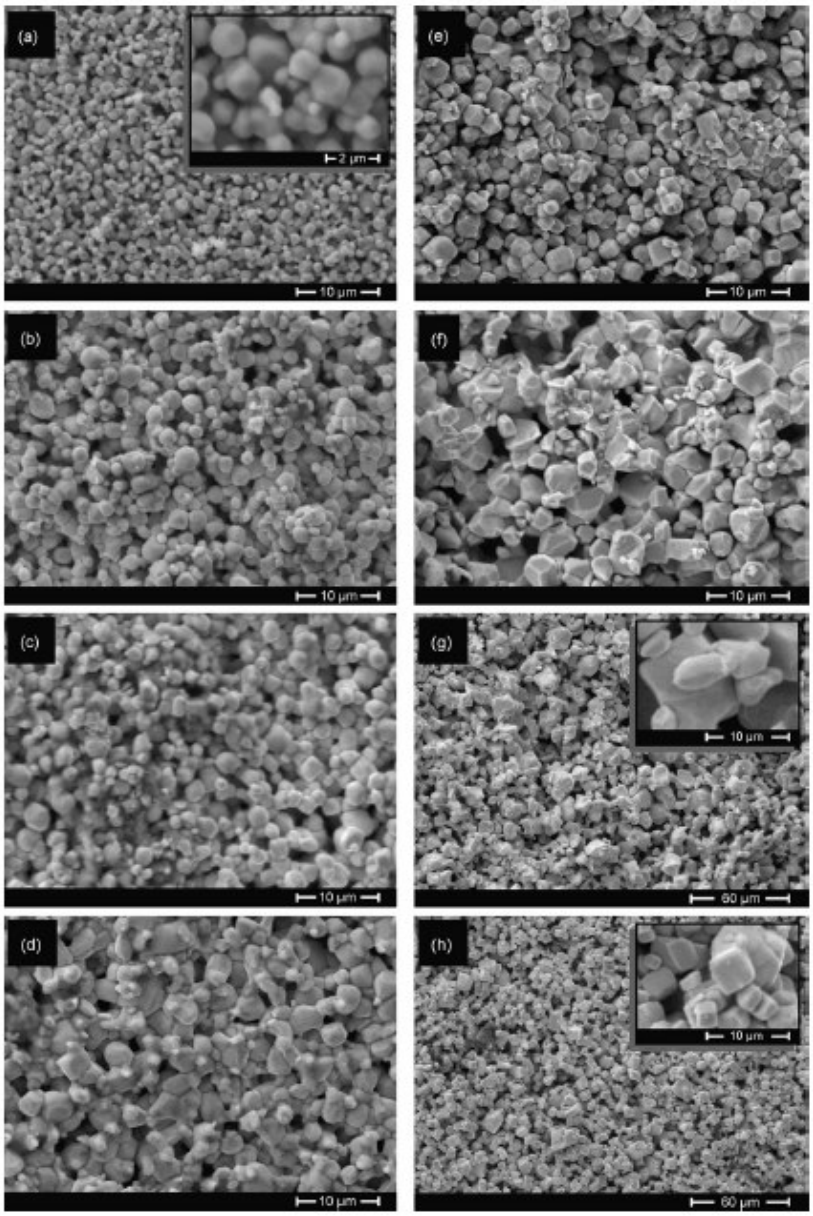

Fig. 8. SEM micrographs of the surfaces of ceramic bodies of **1a** after various sintering temperatures and soaking times. (a) 1450 °C, 1 h; (b) 1550 °C, 1 h; (c) 1600 °C, 1 h; (d) 1650 °C, 1 h; (e) 1550 °C, 10 h; (f) 1600 °C, 10 h; (g) 1650 °C, 10 h; (h) 1500 °C, 30 h.

References

[1] R. Vivekanandan and T. R. N. Kutty, Grain boundary layer ceramic capacitors based on donor-doped $Ba(Ti_{1-x}Sn_x)O_3$. *Mater. Sci. Eng. B*, 1990, **6**[4], 221–231.

[2] Z. G. Zhou, G. Zhao, and M. Wei, Z. T. Zhang, Temperature-humidity-gas multifunctional sensitive ceramics. *Sens. Actuators*, 1989, **19**, 71–81.

[3] P. Singh, B. J. Brandenburg, C. P. Sebastian, P. Singh, S. Singh, D. Kumar, and O. Parkash, Electronic structure, electrical and dielectric properties of $BaSnO_3$ below 300 K. *Jpn. J. Appl. Phys.*, 2008, **47**, 3540–3545.

[4] A. Movchikova, O. Malyshkina, G. Suchaneck, G. Gerlach,R. Steinhausen, H. T. Langhammer, C. Pientschke, and H. Beige, Study of the pyroelectric behavior of $BaTi_{1-x}Sn_xO_3$ piezo-ceramics. *J. Electroceram.*, 2008, **20**, 43–46.

[5] T. Wang, X. M. Chen, and X. H. Zheng, Dielectric characteristics and tunability of barium stannate titanate ceramics. *J. Electroceram.*, 2003, **11**, 173–178.

[6] B. Ostrick, M. Fleischer, U. Hampe, and H. Meixner, Preparation of stoichiometric barium stannate thin films: Hall measurements and gas sensitivities. *Sens. Actuators B*, 1997, **44**, 601–606.

[7] S. Tao, F. Gao, X. Liu, and O. T. Sørensen, Ethanol-sensing characteristics of barium stannate prepared by chemical precipitation. *Sens. Actuators B*, 2000, **71**, 223–227.

[8] U. Lampe, J. Gerblinger, and H. Meixner, Carbon-monoxide sensors based on thin films of $BaSnO_3$. *Sens. Actuators B*, 1995, **24-25**, 657–660.

[9] S. Hodjati, K. Vaezzadeh, C. Petit, V. Pitchon, and A. Kiennemann, NO*x* sorption–desorption study: application to diesel and lean-burn exhaust gas (selective NO*x* recirculation technique). *Catal. Today*, 2000, **59**, 323–334.

[10] P. McGeehin and D. E. Williams, Sensing gaseous substances. Int. Appl., Patent No. WO 9308467 A1 19930429, 1993.

[11] C. V. Gopal Reddy, S. V. Manorama, and V. J. Rao, Preparation and characterization of barium stannate: application as a liquefied petroleum gas sensor. *J. Mater. Sci.:Mater. Electron.*, 2001, **12**, 137–142.

[12] X. Chu, Dilute CH_3SH-sensing characteristics of $BaSnO_3$ thick film sensor. *Mater. Sci. Eng. B*, 2004, **106**, 305–307.

[13] P. H. Borse, J. S. Lee, and H. G. Kim, Theoretical band energetics of $Ba(M_{0.5}Sn_{0.5})O_3$ for solar photoactive applications. *J. Appl. Phys.*, 2006, **100**, 124915–1pp.

[14] P. H. Borse, U. A. Joshi, S. M. Ji, J. S. Jang, J. S. Lee, E. D. Jeong, and H. G. Kim, Band gap tuning of lead-substituted BaSnO3 for visible light photocatalysis. *Appl. Phys. Lett.*, 2007, **90**, 034103–1pp.

[15] Y. Yuan, J. Lv, X. Jiang, Z. Li, T. Yu, Z. Zou, and J. Ye, Large impact of strontium substitution on photocatalytic water splitting activity of $BaSnO_3$. *Appl. Phys. Lett.*, 2007, **91**, 094107–1pp.

[16] H. Mizoguchi, P. M. Woodward, C. Park, D. A. Keszler, Strong near-infrared luminescence in $BaSnO_3$. *J. Am. Chem. Soc.*, 2004, **126**, 9796–9800.

[17] G. Wagner and H. Binder, Untersuchung der binären Systeme BaO-SnO_2 und BaO-PbO_2. I. Phasenanalysen, *Z. Allg. Anorg. Chem.*, 1958, **297**, 328–346.

[18] S. Upadhyay, O. Parkash, and D. Kumar, Solubility of lanthanum, nickel and chromium in barium stannate. *Mater. Lett.*, 2001, **49**, 251–255.

[19] T. R. N. Kutty and R. Vivekanadan, $BaSnO_3$ fine powders from hydrothermal preparations. *Mater. Res. Bull.*, 1987, **22**, 1457–1465.

[20] J. Cerda, J. Arbiol, R. Diaz, G. Dezanneau, and J. R. Morante, Synthesis of perovskite-type $BaSnO_3$ particles obtained by a new simple wet chemical route based on a sol–gel process. *Mater. Lett.*, 2002, **56**, 131–136.

[21] C. P. Udawatte and M. Yoshimura, Preparation of well-crystallized $BaSnO_3$ powders under hydrothermal conditions. *Mater. Lett.*, 2001, **47**, 7–10.

[22] M. Leoni, M. Viviani, P. Nanni, and V. Buscaglia, Low-temperature aqueous synthesis (LTAS) of ceramic powders with perovskite structure. *J. Mater. Sci. Lett.*, 1996, **15**, 1302–1304.

[23] M. T. Buscaglia, M. Leoni, M. Viviani, V. Buscaglia, A. Martinelli, A. Testino, and P. Nanni, Synthesis and characterization of $BaSn(OH)_6$ and $BaSnO_3$ acicular particles. *J. Mater. Res.*, 2003, **18**[3], 560–566.

[24] G. Pfaff, Wet chemical powders synthesis of $BaSnO_3$ and Ba_2SnO_4. *J. Eur. Ceram. Soc.*, 1993, **12**, 159–164.

[25] W. Lu and H. Schmidt, Lyothermal synthesis of nanocrystalline $BaSnO_3$ powders. *Ceram. Inter.*, 2008, **34**, 645–649.

[26] C. P. Udawatte, M. Kakihana, and M. Yoshimura, Preparation of pure perovskite-type $BaSnO_3$ powders by the polymerized complex method at reduced temperature. *Solid State Ionics*, 1998, **108**, 23–30.

[27] W. Lu and H. Schmidt, Synthesis of nanosized $BaSnO_3$ powders from metal isopropoxides. *J. Sol-Gel Sci. Techn.*, 2007, **42**, 55–64.

[28] Y. J. Song and S. Kim, Preparation of $BaSnO_3$ powders by oxalate coprecipitation method. *J. Ind. Eng. Chem.*, 2001, **7**[3], 183–185.

[29] L. Jäger, V. Lorenz, T. Müller, H.-P. Abicht, M. Rössel, and H. Görls, Barium stannate powders from hydrothermal synthesis and by thermolysis of barium-tin(IV)-glycolates. Synthesis and structure of $[Ba(C_2H_6O_2)_4][Sn(C_2H_4O_2)_3]$ and

[$Ba(C_2H_6O_2)_2$][$Sn(C_2H_4O_2)_3$]·CH_3OH. *Z. Anorg. Allg. Chem.*, 2004, **630**, 189–195.

[30] M. D. Aguas, L. Morris, and I. P. Parkin, Self-propagating solid state routes to $BaSnO_3$; investigation of gas sensing properties. *J. Mater. Sci.*, 2002, **37**, 375–379.

[31] A.-M. Azad, L. L. W. Shyan, T. Y. Pang, and C. H. Nee, Microstructural evolution in $MSnO_3$ ceramics derived via self-heat-sustained (SHS) reaction technique. *Ceram. Inter.*, 2000, **26**, 685–692.

[32] R. Köferstein, H.-P. Abicht, J. Woltersdorf, and E. Pippel, Phase evolution of a barium tin 1,2-ethanediolato complex to barium stannate during thermal decomposition. *Thermochim. Acta*, 2006, **441**, 176–183.

[33] R. Köferstein, L. Jäger, V. Lorenz, H.-P. Abicht, J. Woltersdorf, E. Pippel, and H. Görls, Mixed crystalline precursor complexes of the type [$Ba(C_2H_6O_2)_4$][$Ti_{1-x}Sn_x(C_2H_4O_2)_3$] ($x$ = 0–1) for $BaTi_{1-x}Sn_xO_3$ ceramics: Synthesis, structure and calcination. *Solid State Sci.*, 2005, **7**, 1280–1288.

[34] J. W. Price and R. Smith, *Handbook of Analytical Chemistry*, Springerverlag, Berlin-Heidelberg-New York, part III, 1978, vol. 4a, p. 9

[35] K. Kodama, *Methods of Quantitative Inorganic Analysis*, Interscience Publishers, New York, 1963, p. 205

[36] Program WinXPOW v1.06, Stoe & Cie GmbH, Darmstadt (1999).

[37] P.-E. Werner, L. Eriksson, and M. Westdahl, TREOR, a semi-exhaustive trial-and-error powder indexing program for all symmetries. *J. Appl. Cryst.*, 1985, **18**, 367–370.

[38] L. S. Birks and H. Friedman, Particle size determination from X-ray line broadening. *J. Appl. Phys.*, 1946, **17**, 687–692.

[39] R. Köferstein, L. Jäger, M. Zenkner, T. Müller, H.-P. Abicht, Shrinkage mechanism and phase evolution of fine-grain $BaTiO_3$ powder compacts containing 10 mol% $BaGeO_3$ prepared via a precursor route. *Mater. Chem. Phys.*, 2008, **112**, 531–535.

[40] PDF 2 (International Centre for Diffraction Data, Pennsylvania), $BaSnO_3$ [15-780], $BaCO_3$ [5-378]

[41] H. D. Megraw, Crystal structure of double oxides of the perovskite type. *Proc. Phys. Soc., Lond.*, 1946, **58**, 133–152.

[42] J. A. Bearden, X-ray wavelengths. *Rev. Mod. Phys.*, 1967, **39**[1], 78–124.

[43] A. J. Smith and A. J. E. Welch, Some mixed metal oxides of perovskite structure. *Acta Cryst.*, 1960, **13**, 653–656.

[44] H. Jena, K. V. G. Kutty, T. R. N. Kutty, Proton transport and structural relations in hydroxyl-bearing $BaTiO_3$ and its doped compositions synthesised by wet-chemical methods. *Mater. Res. Bull.*, 2004, **39**, 489–511

[45] V. Atakam, C. W. Chen, R. Paul, R. E. Riman, Quantification of hydroxyl content in ceramic oxides: A prompt γ activation analysis study of $BaTiO_3$. *Anal. Chem.*, 2008, **80**, 6626–6632

[46] A. Stashansy, J. Chimborazo, Effect of interstitial hydrogen on structural and electronic properties of $BaTiO_3$. *Phil. Mag.* B, 2002, **82**(10), 1145–1154.

[47] G. Busca, V. Buscaglia, M. Leoni, P. Nanni, Solid-state and surface spectroscopic characterization of $BaTiO_3$ fine powders. *Chem. Mater.*, 1994, **6**, 955–961

[48] K. D. Kreuer, Aspects of the formation and mobility of protonic charge carriers and the stability of perovskite-type oxides. *Solid State Ionics*, 1999, **125**, 285–302

[49] R. Waser, Solubility of hydrogen defects in doped and undoped $BaTiO_3$. *J. Am. Ceram. Soc.*, 1988, **71**(1), 58–63

[50] D. F. K. Hennings, C. Metzmacher, B. S. Schreinemacher, Defect chemistry and microstructure of hydrothermal barium titanate. *J. Am. Ceram. Soc.*, 2001, **84**(1), 179−182

[51] D. Hennings, S. Schreinemacher, Characterisation of hydrothermal barium titanate. *J. Eur. Ceram. Soc.*, 1992, **9**, 41–46.

[52] W. Schatt, *Sintervorgänge*, VDI-Verlag, Düsseldorf, 1992, pp. 78–100.

[53] I. I. Novikov and V. K. Portnoj, *Superplastizität von Legierungen*, Deutscher Verlag für Grundstoffindustrie, Leipzig, 1984, p. 12 et seqq..

[54] D. Völtzke and H.-P. Abicht, The influence of different additives and the mode of their addition on the sintering behavior and the properties of semiconducting barium titanate ceramics. *Solid State Sci.*, 2000, **2**, 149–159.

[55] M. N. Rahaman, *Ceramic proceeding and sintering*, ed. Marcel Dekker, New York, 1995, pp. 398 et seqq.

[56] Y. Dror, R. D. Levi, S. Baltianski, and Y. Tsur, Identification of the early stage of sintering of nano-$BaTiO_3$. A comparative study. *J. Electrochem. Soc.*, 2006, **153**[7], F137–F143.

[57] W. Schatt, Vorgänge beim Festphasensintern und ihre Verallgemeinerungsfähigkeit. *Z. Metallkde.*, 1989, **80** [11], 809–816.

[58] Ya. E. Geguzin and Yu. I. Klinchuk, Mechanism and kinetics of the initial stage of the solid-phase sintering of pressed parts from crystal-body powders activity during sintering. *Poroshkovaya Metallurgiya*, 1976, **7**, 17−25.

[59] W. Schatt, Study of sintering processes by positron annihilation. *Solid State Phenomena*, 1992, **25-26**, 23–28.

[60] S. Upadhyay, O. Parkash, and D. Kumar, Preparation and characterisation of barium stannate $BaSnO_3$. *J. Mater. Sci. Lett.*, 1997, **16**, 1330–1332.

[61] A.-M. Azad, M. Hashim, S. Baptist, A. Badri, A. Ul. Haq, Phase evolution and microstructural development in sol-gel derived $MSnO_3$ (M = Ca, Sr and Ba). *J. Mater. Sci.*, 2000, **35**, 5475–5483.